Nozzle Side Load Testing and Analysis at Marshall Space Flight Center

Joseph H. Ruf [1], David M. McDaniels[2] Andrew M. Brown[3]
NASA Marshall Space Flight Center, Huntsville, Alabama 35812

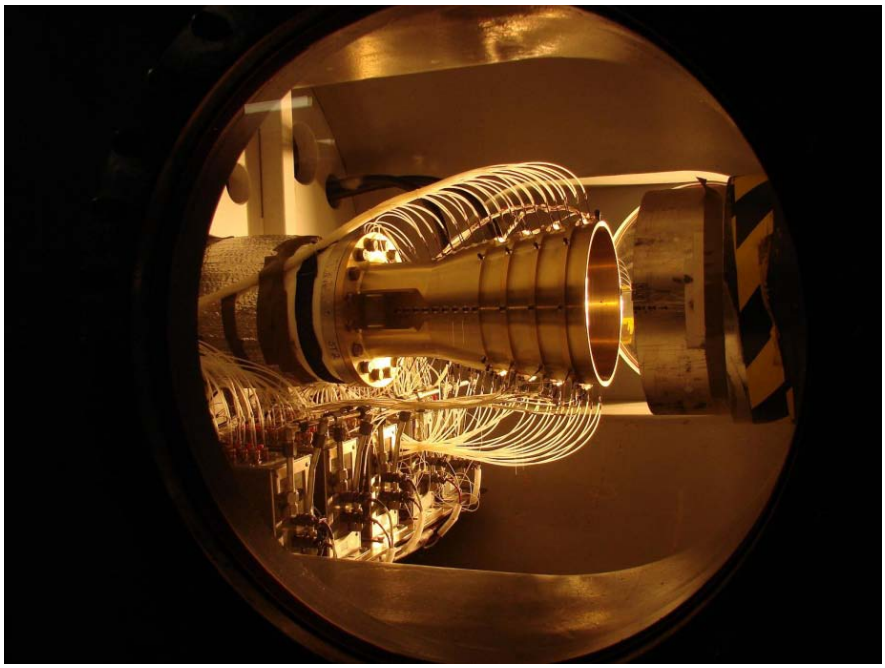

A Cold Flow Nozzle Test Article in MSFC's Nozzle Test Facility

Realistic estimates of nozzle side loads, the off-axis forces that develop during engine start and shutdown, are important in the design cycle of a rocket engine. The estimated magnitude of the nozzle side loads has a large impact on the design of the nozzle shell and the engine's thrust vector control system. In 2004 Marshall Space Flight Center (MSFC) began developing a capability to quantify the relative magnitude of side loads caused by different types of nozzle contours. The MSFC Nozzle Test Facility was modified to measure nozzle side loads during simulated nozzle start. Side load results from cold flow tests on two nozzle test articles, one with a truncated ideal contour and one with a parabolic contour are provided. The experimental approach, nozzle contour designs and wall static pressures are also discussed.

[1] Aerospace Engineer, ER42/Fluid Dynamics Branch, AIAA Member
[2] Aerospace Engineer, ER42/Fluid Dynamics Branch
[3] Lead Aerospace Engineer, ER41/Propulsion Structural & Dynamics Analysis Branch, AIAA Senior Member

Nomenclature

F = Side Load Force
F_{NPR} = Side Load Force as Function of NPR
FSS = Free Shock Separation
G_{NPR} = Side Loads Scalar Relationship
H_{NPR} = Side Load Scalar Moment Relationship
M_{NPR} = Moment as function of NPR
NPR = Nozzle Pressure Ratio, P_c/P_{amb}
NTF = Nozzle Test Facility
P_c = Nozzle Total Pressure
P_w = Nozzle Wall Pressure
P_{amb} = Ambient Pressure
PAR = Parabolic
qRSS = quasi-Restricted Shock Separation
RSS = Restricted Shock Separation
TIC = Truncated Ideal Contour

I. Introduction

NOZZLE side loads are lateral forces induced by asymmetric pressure distribution in a nozzle. The most severe nozzle side loads occur during the engine start and shutdown transients as the plume fills and then empties from the nozzle. Two common engine failure modes due to side loads are nozzle wall high-cycle fatigue and over loading the engine thrust vector control actuator. Most liquid rocket engines have, at one time or another, had issues due to nozzle side loads. The J-2S had excessive side loads such that an entire engine was ripped from its gimbal structure. The Space Shuttle main engine had side load induced nozzle coolant line (the "steer-horn") fatigue cracks. More recently, the Japanese LE-7A engine had problems due to nozzle side loads during development.[1]

The European liquid rocket engine, the Vulcain, experiences significant side loads as well.[2] In the 1990's several European organizations joined together as the Flow Separation Control Devices research group to address nozzle side loads. Several experimental and analytical programs were completed that provided new and valuable insight into the nozzle fluid dynamics that are responsible for nozzle side loads.[3,4] However, in the U.S., there was no organized program addressing liquid rocket nozzle side loads.

The work described in this paper are results from an MSFC internally funded effort begun in 2004 to develop, within the U.S., a nozzle side load test capability and the experience and knowledge base to support future liquid rocket nozzle development. The specific objective of this cold flow test campaign was to determine the relative magnitude of nozzle side loads for two test articles; a truncated ideal contoured (TIC) nozzle and a thrust optimized contour, specifically a parabolic (PAR), nozzle. The side load of interest was the net throat bending moment (Fig. 1) during start and shutdown transients.

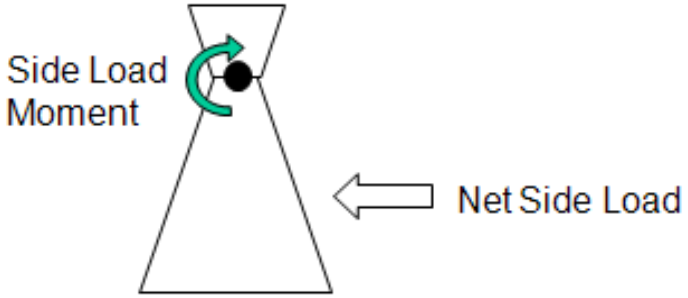

Figure 1. Throat bending moment due to side load.

II. Nozzle Fluid Dynamics

A brief and very basic explanation of the nozzle fluid dynamics that contribute to nozzle side loads follows. Several of the references provide a fuller explanation of nozzle fluid dynamics during start and shutdown. The reader is directed specifically to references 5, 6, 7, 8, and 4.

The key difference between the TIC and PAR nozzles is the presence of an internal shock (see Fig. 2) in the PAR due to the non-ideal nozzle wall curvature just downstream of the throat. At low nozzle pressure ratio, P_c/P_{amb}, (NPR) this internal shock interacts with the separation induced shock (NPR 16, Fig. 2) and then the Mach disk (starting at NPR 20 in Fig. 2) as the NPR increases. If the internal shock is strong, its interaction with the Mach disk can cause the annular supersonic plume to deflect outward and reattach to the nozzle wall (NPR 21, Fig. 2). The reattachment results in a recirculation bubble, "restricted", between the separation location and the reattachment location. This transition to reattached flow, i.e., from free shock separation (FSS) to restricted shock separation (RSS), is one source of large nozzle side loads when the transition is nonsymmetric. A second source of large side loads is when the RSS reattachment location is near the end of the nozzle. The plume will flip back and forth between FSS and RSS as the separation approaches the nozzle exit plane.

Conversely, the TIC flow remains in FSS throughout the nozzle start transient (except at very low NPRs) as indicated in the images on the left hand side of Fig 2. This continuous FSS flow in the TIC produces significantly lower side loads than the FSS-to-RSS-to-FSS transitions that are possible in a thrust optimized contoured nozzle.

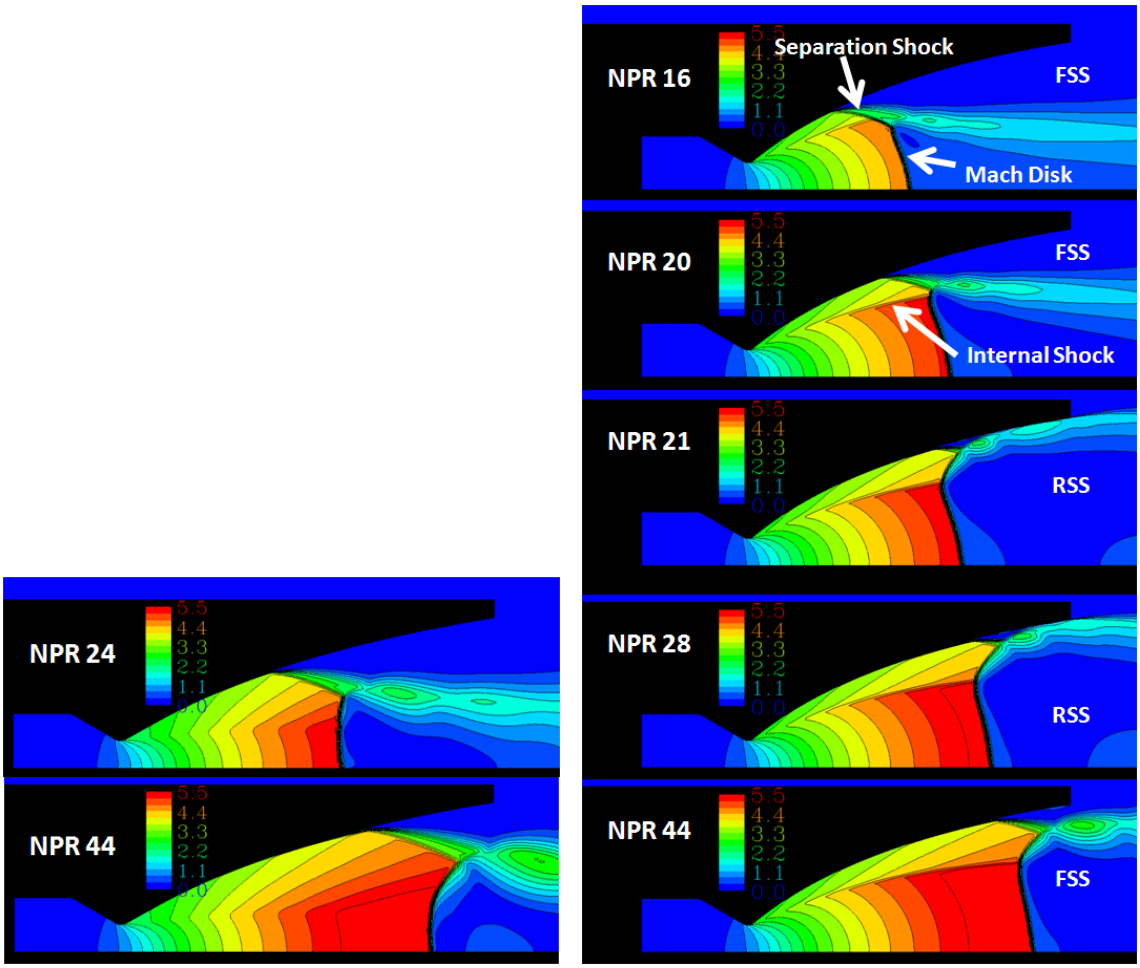

Figure 2. Computational fluid dynamic solutions for the TIC test article (left) at two NPRs and the PAR test article (right) at five NPRs.

III. Experimental Approach

The test approach implemented here was proposed by Dumonv[9] and further developed by Frey[10], et al. The test articles were mounted on a flexible, easy-to-characterize "strain tube" (Fig. 3). Moments due to off-axis forces were measured with strain gages near the rigidly mounted end of the tube. Two pairs of full-bridges were applied to measure strain in both the horizontal and vertical directions. The nozzle test articles were designed to be relatively stiff. Their throat bending and nozzle ovalization fundamental frequencies were well above the expected excitation frequency range (0-300 Hz) from side loads.

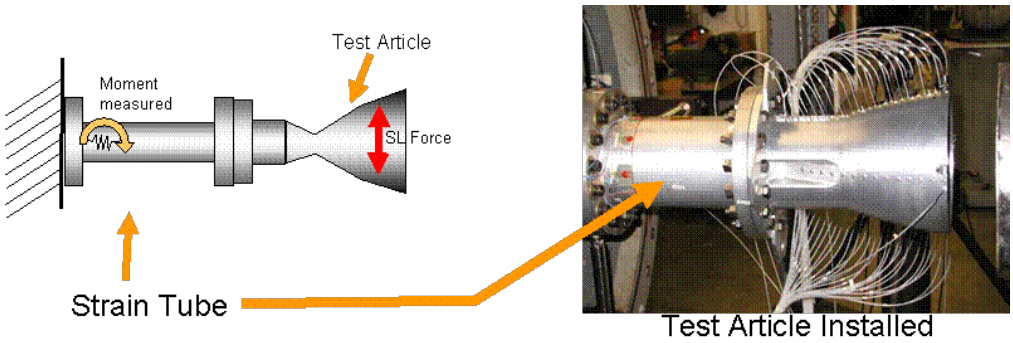

Figure 3. Schematic of the strain tube approach and a picture of the strain tube and a test article installed.

A. Running Tests

The MSFC Nozzle Test Facility (NTF), Fig 4, was designed to determine nozzle thrust efficiencies over a range of simulated altitudes. The nozzle working gas is heated dry air at pressures up to 20 atm. Typical run conditions are nozzle total pressure of 10.2 atm (150psia) at 66°C (150°F). The NTF's two stage ejector system can pull the vacuum chamber pressure down to simulated altitudes greater than 30km (100,000ft).

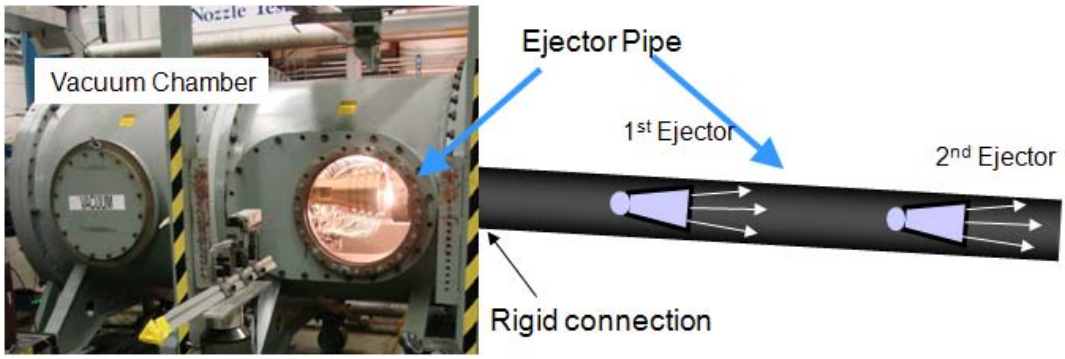

Figure 4. The NTF vacuum chamber with a nozzle test article installed.

For side load testing the thrust measurement system was removed and the test article support was stiffened to provide a rigid mount for the strain tube. Typical operating procedure in this side load testing was to bring the nozzle test article chamber to set point, 10.2 atm, 66°C, without the ejectors running. This set point is maintained throughout the test. Before the ejectors were turned on the NPR (where P_{amb} is the vacuum chamber pressure) was about 12 resulting in the nozzle flow separating just downstream of the throat. The ejectors were then brought on quickly to drop the vacuum chamber pressure low enough to induce the nozzle test article to flow full. The ejectors were then shut down and the vacuum chamber returned to near atmospheric pressure. This cycle was repeated, as many as 35 times in one "test", until the ejector drive gas ran low. A plot of NPR v. time for a typical test is shown in Fig. 5. The timing between the two ejector start commands and rate at which they were ramped up were varied to achieve a variety of NPR ramp rates. Figure 6 provides an example of typical NPR ramp rates.

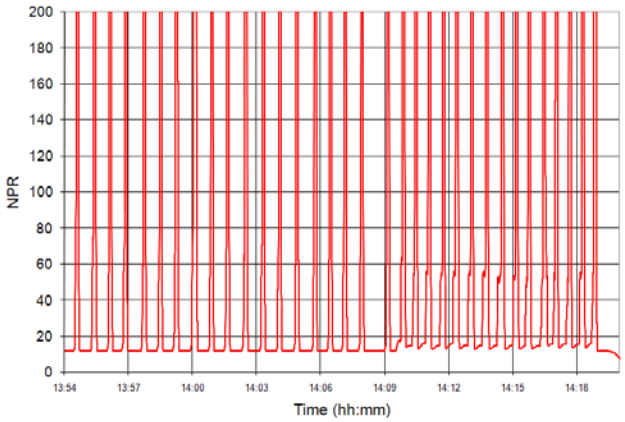

Figure 5. Example of NPR ramps in one test cycle.

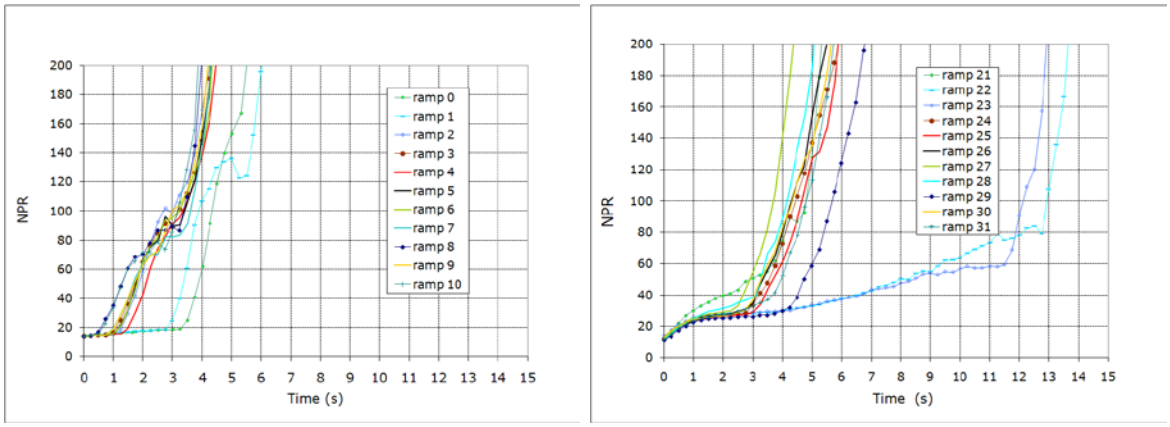

Figure 6. Example NPR ramp rates achieved.

One of the limitations of using a vacuum chamber is that nozzle shutdown cannot be properly simulated. The exit plane of the nozzle test article is relatively close to the ejector pipe inlet as indicated in Fig. 4. Decreasing NPR, with constant nozzle total pressure requires increasing the vacuum chamber pressure. Increasing the vacuum chamber pressure requires mass to flow back into the vacuum chamber through the ejector pipe. This mass flow buffeted the nozzle producing a load source other than those from nozzle flow separation.

The data discussed in this paper was obtained in two tests of 35 simulated nozzle starts for both the TIC and PAR nozzle test articles, resulting in a total of 70 simulated starts for each nozzle.

B. Nozzle Test Article Design

The test articles (Fig. 7) were fabricated from aluminum. They both have an area ratio of 30.5 to 1, with a throat diameter of 38.1mm (1.5in). The test articles have the same mass and center of gravity so that the strain tube and nozzle system has the same response with both nozzles. Static and high frequency pressure ports were machined into the nozzles as indicated in Fig. 7. The high frequency pressure measurements were not made in this test series. Those instrumentation ports were filled with machine screws such that the end of the screw was flush with the nozzle contour.

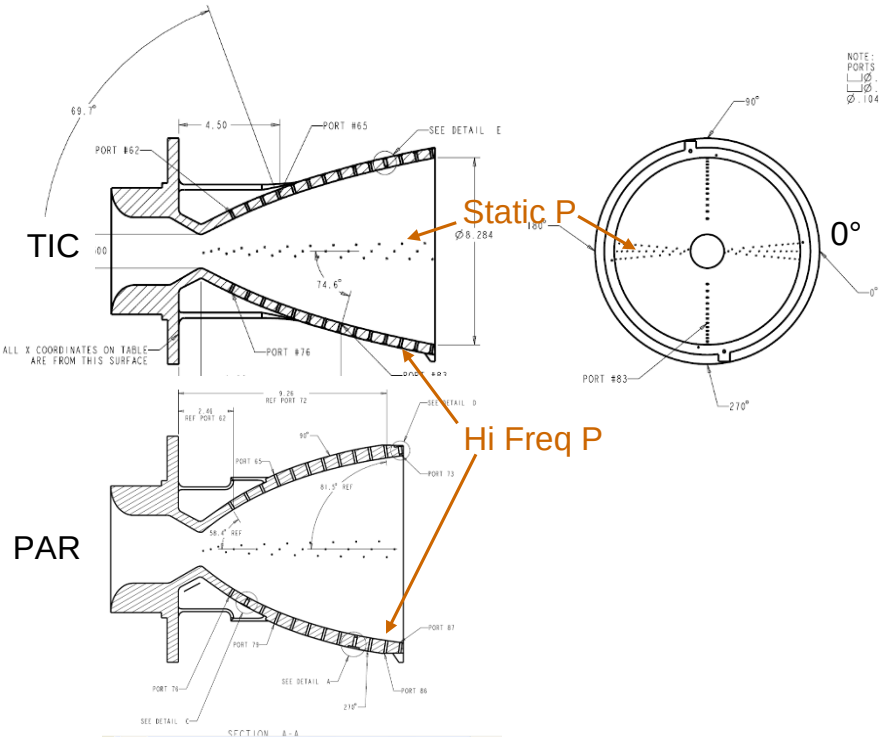

Figure 7. Cross-sections of the TIC and PAR nozzle test articles.

The TIC and PAR contours and as-designed nozzle wall pressures are shown in Fig. 8. The TIC test article contour was developed by first calculating a full length ideal contour with an ideal bell nozzle code[11]. That contour was then truncated at 79% length of an equivalent 15° conical nozzle of the same area ratio. The truncation length was chosen so the desired nozzle wall pressure ratio, $P_w/P_c = 2.5x10^{-3}$, existed at the exit. This nozzle wall exit pressure ratio was desired because it would result in nozzle flow separations over a range for which the NTF vacuum chamber pressure was easy to control.

The PAR nozzle contour was developed using the skewed parabola option in the TDK02[12] design and analysis tool. The throat expansion angle, 40°, was chosen higher than might otherwise be typical for a thrust optimized nozzle. Being the first, and possibly only, thrust optimized contour test article to be fabricated it was desired that the PAR test article definitely have the transition to RSS. The high initial throat angle would ensure this development task was able to measure and compare side loads of a TIC nozzle contour without the FSS-to-RSS transition to side loads of a thrust optimized nozzle contour with FSS-to-RSS transition.

The PAR length and contour exit angle were adjusted so that the transition to RSS would occur at an NPR that was neither too low nor too high. This last judgment was subjective. Computational fluid dynamic simulations performed during the test article design phase indicated the transition to RSS would occur at NPR of about 24.

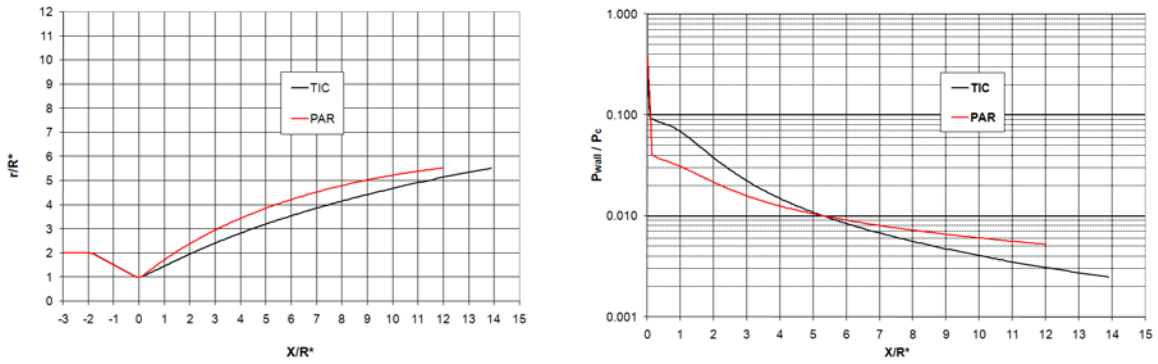

Figure 8. Nozzle test article contours (left) and as-designed wall pressures (right).

C. Calibration of the Strain Gages and Filtering

Calibration of the strain gages was achieved by hanging weights from a system of knife edges and pulleys designed such that pure horizontal and vertical static loads were applied. These loads produced a moment and a measureable strain at the strain gage location. A full factorial experimental design was used, providing every combination of loads in a 2-factor, 5-level matrix. Strain tube temperature was carefully maintained with a small flow of temperature controlled air through the strain tube during the calibration process. This calibration data (a response surface using multiple linear regressions) was then used to calculate the moment in both directions as a function of the strain gage measurements.

The TIC and PAR test articles were designed to have the same masses and centers of gravity so that when mounted on the strain tube the strain tube/nozzle system would have the same fundamental frequencies. The fundamental frequency for the strain tube/TIC nozzle system was 207.5Hz and for the strain tube/PAR nozzle system it was 215Hz. This small difference in frequency can be attributed to the differences in instrumentation between the test articles. Note that these frequencies were within the range of expected side load excitation frequencies. This was a design compromise made early on to ensure the strain induced in the tube was sufficiently large to be measured accurately. The effect on the strain gage frequency domain is shown in Fig. 9. The black lines show peaks due to resonance at their respective fundamental frequencies.

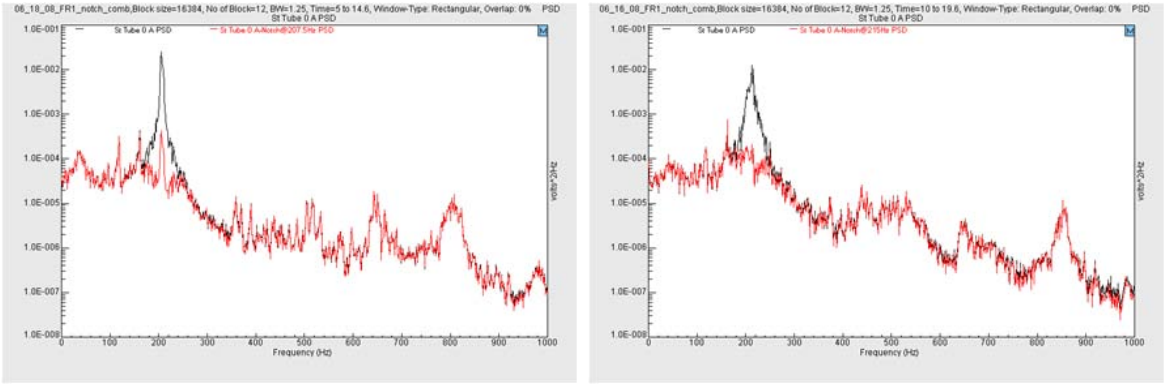

Figure 9. Frequency content of the strain gage signal of TIC (left) and PAR (right) before (black) and after (red) filtering.

The strain gage measurements reflect the equivalent, instantaneous static load on the tube. Since the actual load is extremely dynamic and excites the resonant frequency of the strain tube/nozzle system, the strain gage measurement, without a correction, would have been a largely inaccurate measurement of the load. It was determined that if the system resonance effect was filtered out, the remaining part of the strain gage signal was essentially equal to the static loading due to the aerodynamic side load forces[13]. To further reduce the impact of system dynamics on the conclusions drawn from the test data the filtered side load moments were normalized by the maximum measured moment (from the filtered data). This normalizing of the data determines the relative magnitude of side load moments for the two nozzle contours over their start transients.

The filter applied to remove the effect of the resonance from the strain gage signal was a “notch” filter, 45 Hz wide. The width of the filter was selected by examining the response power spectral densities. The value of ±22.5 Hz around the resonant peak spanned the region in which the response appeared to be magnified by the resonance. The red lines in Figure 9 show the effect of the 45 Hz-wide notch filter on the strain gage signal. Further details of the effort to determine the true value of the aerodynamic force (the side load) from the test data can be found in reference 13.

The strain gage signals and nozzle total and vacuum chamber pressures were recorded at 20,000 Hz. After filtering, the strain gage data, nozzle total pressure and vacuum chamber pressure were imported into MATLAB. The calibration equations were applied to the strain gage signals and the NPR was calculated for each of the 20,000 measurements per second. To make the volume of data more manageable the data was grouped into different “bins” of NPR (Table 1). The side load maximum, minimum, average and standard deviation of each NPR bin for each simulated nozzle start were calculated.

Table 1. Bins of NPR

bin minimum	bin center	bin maximum		bin minimum	bin center	bin maximum
12.0	13.0	14.0		61.0	62.5	64.0
14.0	15.0	16.0		64.0	66.0	68.0
16.0	17.0	18.0		68.0	70.0	72.0
18.0	19.0	20.0		72.0	74.0	76.0
20.0	21.0	22.0		76.0	78.0	80.0
22.0	23.0	24.0		80.0	82.0	84.0
24.0	25.0	26.0		84.0	86.0	88.0
26.0	27.0	28.0		88.0	90.0	92.0
28.0	29.0	30.0		92.0	94.0	96.0
30.0	31.0	32.0		96.0	98.0	100.0
32.0	33.0	34.0		100.0	102.5	105.0
34.0	35.0	36.0		105.0	107.5	110.0
36.0	37.0	38.0		110.0	112.5	115.0
38.0	39.0	40.0		115.0	117.5	120.0
40.0	41.5	43.0		120.0	122.5	125.0
43.0	44.5	46.0		125.0	127.5	130.0
46.0	47.5	49.0		130.0	132.5	135.0
49.0	50.5	52.0		135.0	137.5	140.0
52.0	53.5	55.0		140.0	142.5	145.0
55.0	56.5	58.0		145.0	147.5	150.0
58.0	59.5	61.0		150.0	152.5	155.0

IV. Results

A. Nozzle Wall Static Pressure

Nozzle wall static pressures were recorded at 4 Hz. To obtain the static pressure profiles the NPR was held constant or the ramp rate was significantly reduced from that shown in Fig. 5. Figure 10 presents the TIC test article's wall pressure data in two nondimensional forms. The profiles show the typical FSS characteristics of a TIC nozzle; a sharp rise in the wall pressure at the separation point, a plateau pressure close to P_{amb} and then disappearance of the plateau as the separation point approaches the nozzle exit plane.

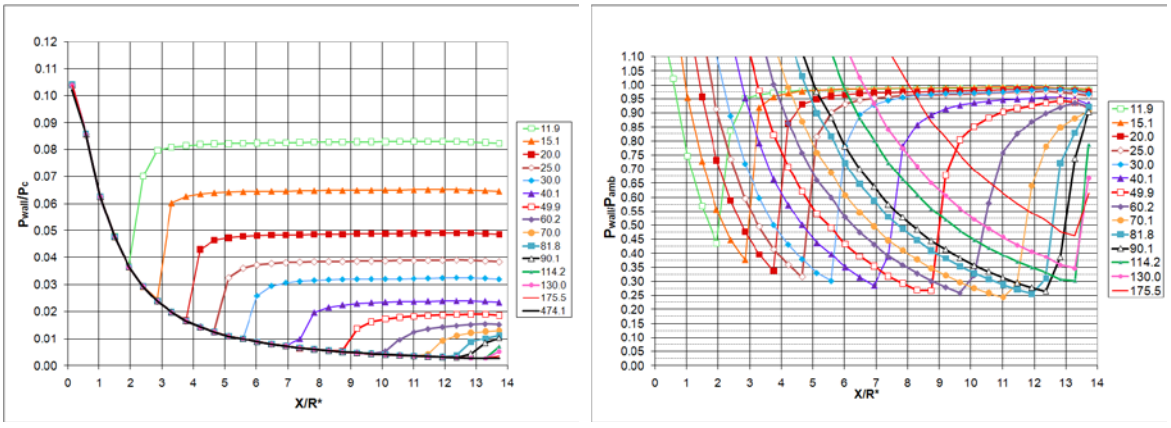

Figure 10. TIC nozzle wall pressure normalized.

Figure 11 presents the PAR test article's wall pressure data for increasing NPR. These profiles exhibit FSS-to-RSS-to-FSS characteristics of thrust optimized contour nozzles. The nozzle flow was in FSS up to NPR 23.7 and transitioned consistently to RSS at NPR 23.8. From there up to an NPR of just above NPR 57.2 the nozzle wall pressures had peaks well above P_{amb} and troughs that came back down to just below P_{amb}. Above NPR 57.2 the PAR flow was in FSS up to approximately NPR 65 where it flowed full.

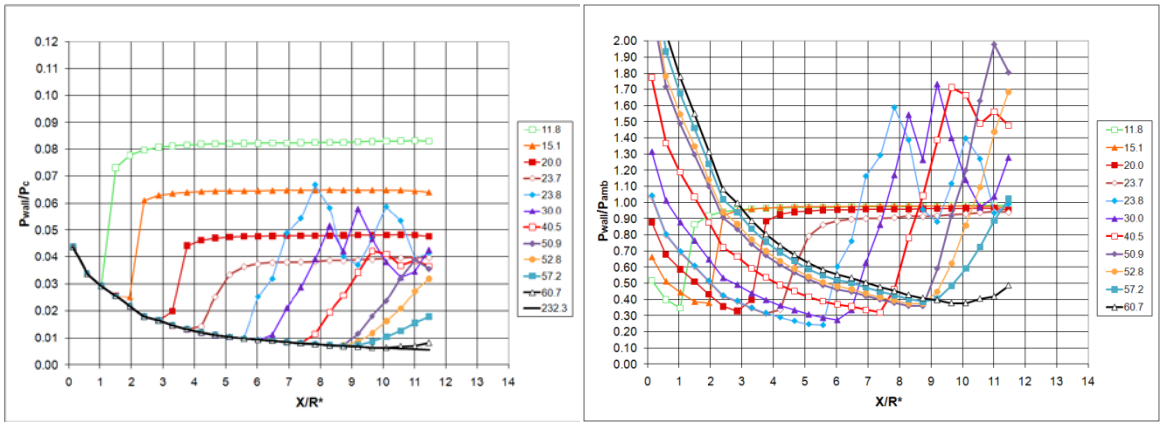

Figure 11. PAR nozzle wall pressure normalized. Increasing NPR.

Figure 12 presents the PAR test article's wall pressure data for decreasing NPR. The PAR test article flowed full down to NPR 62.2. Between NPR 62.2 and approximately 57.5 it was in FSS. From NPR 57.5 down to NPR 13.4 the PAR test article's plume remained in RSS. Slightly below NPR 13.4 the PAR test article plume transitioned back to FSS. During RSS the peaks in the wall pressure profiles were again well above P_{amb} and troughs were near P_{amb}. This hysteresis in transition, FSS-to-RSS at 23.8 during increasing NPR and RSS-to-FSS at NPR 13.4 during decreasing NPR, is typical behavior of nozzles with RSS flows. Note that for those NPRs in which the flow is in RSS, NPRs from the mid-20s to mid-50s, the pressure profiles are quite similar for increasing and decreasing NPRs.

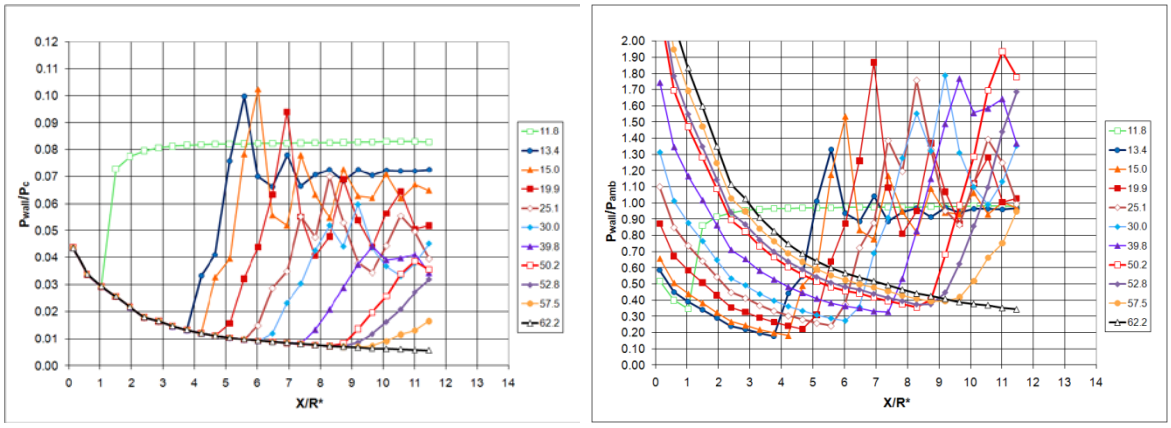

Figure 12. PAR nozzle wall pressure normalized. Decreasing NPR.

B. Side Load Moments Unscaled

As discussed previously, the 20,000 Hz strain gage data was filtered and converted to a moment and collected in bins of NPR (Table 1) for each simulated nozzle start transient. The maximum side load moment in each bin over the approximate 70 starts for both nozzles is plotted in Fig 13. This data was normalized by the maximum moment measured for the PAR nozzle.

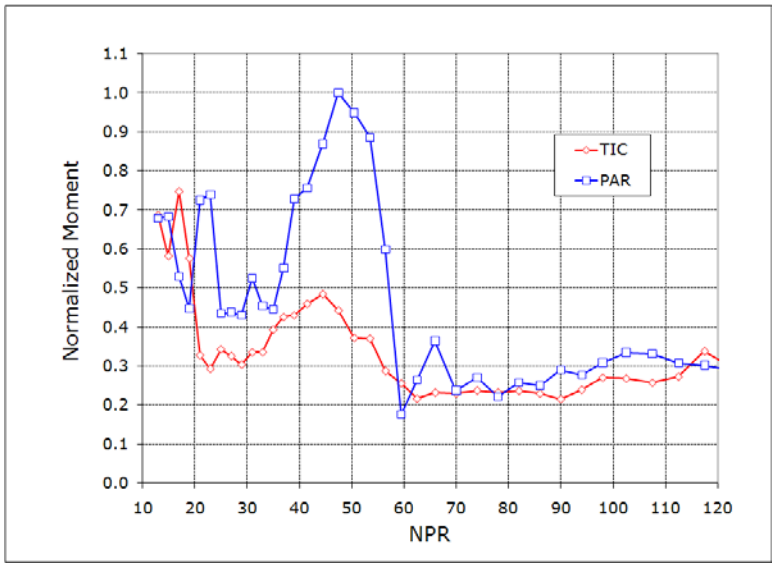

Figure 13. Relative side load of TIC and PAR nozzles.

Both nozzles had two peaks in side load moment: one at low NPR and one at a mid-range NPR. The maximum side load moment of the PAR nozzle, at NPR 47.5, was significantly higher than either of the peak moments from the TIC nozzle. The maximum moment of the PAR nozzle occurred as the RSS separation bubble reached the end of the contour. Highly oscillatory flow existed as the nozzle flow transitioned back and forth rapidly between RSS and FSS. Conversely, the maximum side load moments of the TIC nozzle at NPRs in the mid-40s were due only to FSS separation line oscillation. This conclusion was drawn from observations of the Schlieren video and high frequency pressure measurements made in another test series on these same test articles. After the nozzles flowed full, above a NPR of about 60, the side load moments of both decreased significantly. The moments present at the higher NPRs on Fig 13 were similar to those obtained from a reference, sonic nozzle. The sonic nozzle produced no aerodynamic side loads; therefore, the moments measured during the sonic nozzle tests were a measure of the facility effects (i.e., random noise) in the test data.

The peaks in side load moment at low NPRs for the two nozzles were very similar in magnitude. However, the low NPR peak were, in part, due to different fluid dynamics. The PAR nozzle had two peaks at low NPR. The first, at NPR 13, was probably due to transition from FSS to a flow state called "quasi-RSS"[14] (qRSS). qRSS is a short-lived asymmetric flow reattachment that can occur as the plume expands just past the throat. The second low NPR peak for the PAR nozzle, at NPRs 21 and 23, was a result of the FSS-to-RSS transition. The peak in the TIC's side load moments at NPR 17 was most likely due to FSS-to-qRSS-FSS flow transitions.

C. Scaling for Ambient Pressure

In this test approach, the nozzle total pressure was held constant and the NTF vacuum chamber was evacuated to increase NPR, thereby, inducing the nozzles to flow full. In doing so, the vacuum chamber pressure, P_{amb} for the nozzles, dropped from near atmospheric to well below 0.05 atm. The result was that the magnitude of the aerodynamic force produced by any asymmetric separation decreased with increasing NPR. Therefore, a relationship was required to scale the measured side load moments to the normal operating procedure for nozzle transients, where P_c increases against a constant P_{amb}.

In general the lateral forces due to an overexpansion are a function of the nozzle P_c, the nozzle P_w distribution, the wall surface area and P_{amb}. Figure 14 is a simplified schematic of the aerodynamic forces resulting from

asymmetric filling of a nozzle. This simplistic, two-dimensional representation of asymmetric separation is used here to show that nozzle side loads scale linearly with P_{amb}.

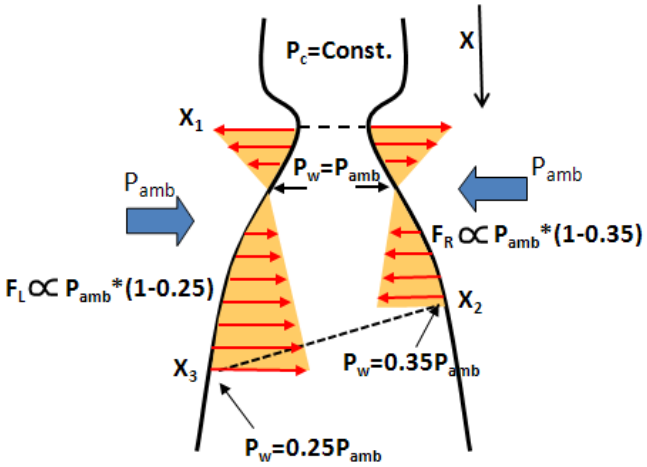

Figure 14. Simple schematic of the aerodynamics forces that cause side loads.

In this schematic the flow separates on the left side of the nozzle where the wall pressure is 0.25 of P_{amb}. On the other side of the nozzle the flow separates where the wall pressure is 0.35 of P_{amb}. The lateral force, or side load, generated on the left side of the nozzle, F_L, is the product of the wall surface area, A, and the difference between P_w and P_{amb} from the throat, down through the over the overexpanded length the point of separation.

$$F_L = \int_{x_1}^{x_3} A_i \, (P_{w_i} - P_{amb}) \tag{1}$$

The region downstream of the separation should also be included, but the same principles apply over that region. The region downstream of the separation is not included here for simplicity sake.

Likewise, the lateral force on the right side, F_R, is:

$$F_R = \int_{x_1}^{x_2} A_i \, (P_{w_i} - P_{amb}) \tag{2}$$

However, between axial stations X_1 and X_2 the forces offset each other such that the net lateral force, i.e., the side load, F, is:

$$F = \int_{x_2}^{x_3} A_i \, (P_{w_i} - P_{amb}) \tag{3}$$

At this point the reader is reminded that in the vacuum chamber test approach the nozzle P_c does not vary with time. This, in turn, means that the P_w in the non-separated regions of the nozzle is always the same. For the nozzle flow as depicted in Fig. 14 equation 3 can be written as:

$$F = \int_{x_2}^{x_3} A_i \, P_{amb} \left(\frac{P_{w_i}}{P_{amb}} - 1 \right) \tag{4}$$

where the values of P_{wi}/P_{amb} between X_2 and X_3 are constants of 0.35 and 0.25, respectively. Recognizing the integral of A_i is also a constant, allows equation 4 to be expressed as:

$$F_{NPR} = P_{amb\ NPR} \int_{x_2}^{x_3} A_i \left(\frac{P_{w_i}}{P_{amb\ NPR}} - 1 \right) = P_{amb\ NPR}\, G_{NPR} \tag{5}$$

with the "NPR" subscript here indicating the values are a function of NPR. G_{NPR} is everything inside the integral:

$$G_{NPR} = \int_{x_2}^{x_3} A_i \left(\frac{P_{w_i}}{P_{amb\ NPR}} - 1 \right) \tag{6}$$

Recognize that at a particular time, or NPR, in a nozzle transient that the right hand side of equation 6 is a constant. Equation 5 can be rearranged to give:

$$G_{NPR} = \frac{F_{NPR}}{P_{amb\ NPR}} \tag{7}$$

and if, as tested here, the moment is measured, equation 7 can be written as:

$$H_{NPR} = \frac{L_{NPR} F_{NPR}}{P_{amb\ NPR}} = \frac{M_{NPR}}{P_{amb\ NPR}} \tag{8}$$

where L_{NPR} is the moment arm and M_{NPR} is the moment at a given NPR.

In equation 8, H_{NPR} is the scalar constant relationship between the side load moment and P_{amb} for that particular point (i.e. NPR) in the nozzle transient. If one considers the range of NPRs over the nozzle start transient, the side load moment at each NPR could be normalized by the P_{amb} at that same NPR which means H_{NPR} would then be a scalar function relationship between the moment and P_{amb} over the entire nozzle transient.

Equation 8 shows that the magnitude of the side load moment is linearly related to the ambient pressure by some function over a range of NPRs. This function, H_{NPR}, encompasses the integration of the asymmetric, overexpanded wall pressure and the wall pressures downstream of the separation. Equation 8 was arrived at by considering the forces in a simple two dimensional separated flow at one point in time. The same result, i.e., the side force is linearly proportional to P_{amb}, could also be arrived at for an axisymmetric nozzle with highly complex separation patterns.

Determining H_{NPR} (or G_{NPR}) analytically is difficult, however, the experimental work here provides an experimental evaluation of moments for both nozzles. With equation 8 the moments measured in the MSFC NTF (Fig. 13) can be scaled by a P_{amb} of 1atm. The moment for each NPR bin was scaled by the P_{amb} that corresponds to the bin center NPR listed in Table 1. These scaled moments are discussed in the next section.

An assumption made in the derivation of equation 8 is that the separation characteristics do not change with different Reynolds numbers.

D. Side Load Moments After Scaling

Figure 15 presents the normalized side load moments after they were scaled for the effect of P_{amb} per equation 8. The PAR's maximum side load moment, after scaling, was at NPR 50.5 and the TIC's was still at NPR 44.5. The magnitude of the maximum side load moment of the TIC nozzle was 45% of the PAR nozzle's maximum moment. The low NPR side load moments, when scaled, were significantly lower than their respective maximum side loads at the mid-range NPRs. Note that the side load moments induced by the PAR nozzle's FSS-to-RSS transition and the TIC nozzle's FSS-to-qRSS-to-FSS are still apparent.

The scaling factor was not applied to the measured side load moments for the PAR and TIC nozzles above NPRs 66 and 86, respectively. In another test series, high frequency pressure measurements were obtained near the nozzle exit planes. NPRs 66 and 86 were the highest NPRs in which the high frequency wall pressure indicated any separation, no matter how short-lived or weak. Above these NPRs the nozzles were flowing completely full meaning any measured moments were not due to separated flow, and therefore, no scaling should be applied.

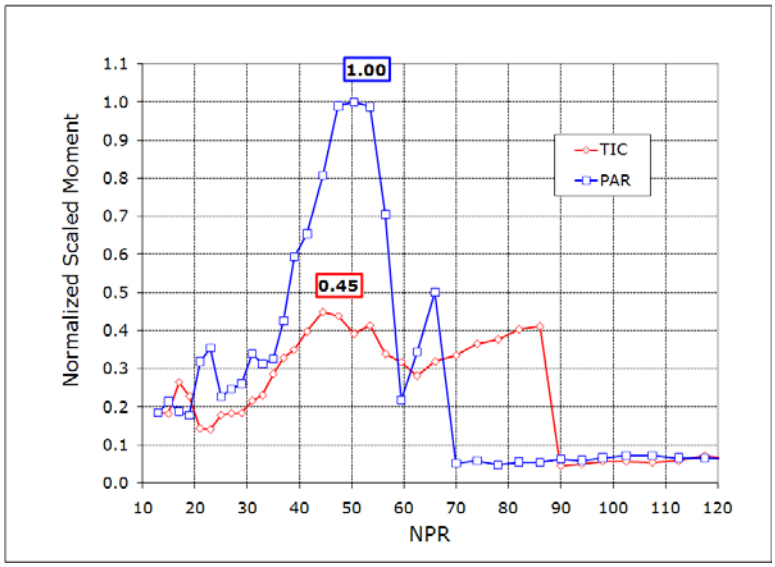

Figure 15. Relative side load after scaling for P_{amb}.

V. Conclusions

The strain tube side load measurement approach was successfully implemented in MSFC's Nozzle Test Facility for nozzle start transients. Two cold flow nozzle test articles were developed, a truncated ideal and a parabolic contour, which produced the desired types of nozzle flows. The truncated ideal contour test article's wall static pressures and side load moments exhibited FSS behavior expected for truncated ideal nozzles. The parabolic contoured nozzle test article's wall static pressures and side load moments indicated transitional nozzle flow behavior, FSS-to-RSS-to-FSS, typical of thrust optimized contours. During simulated nozzle start transients, the maximum side load magnitude of the truncated ideal contour test article was 45% of that of the parabolic contour test article.

Acknowledgments

The authors would like to thank the entire cold flow nozzle test team (Fig. 16) for their contribution to this task. The authors would also like to thank Roberto Garcia and Bruce Tiller, both of MSFC, for their continual support for this task during its formative stage.

Figure 16. The NTF nozzle side load team. Front row, left to right, Tim Karigan, Joe Ruf, Andy Brown, Al Mayer, Martin Cousins, Back Row, Jim Sieja, Doug Counter and Dave McDaniels. Not pictured: Kris McDougal and Dick Branick.

References

1. Wantabe, Y.; Sakazume, N.; and Tsuboi, M.: "LE-7A Engine Nozzle Problems During the Transient Operations," *AIAA Paper No. 2002-3841*, July 2002.
2. Hagemann, G.; et al.: "Flow Separation and Side-Loads in Rocket Nozzles," Paper at the 4th International Symposium Rocket Space Propulsion, March, 2000. Lampoldshausen, Germany.
3. Ostlund, J.; et al.: "Side Load Phenomena in Highly Over-Expanded Rocket Nozzles," *AIAA Paper No. 2001-3684,* July 2001.
4. Terhardt, J.; and Hagemann, G.: "Flow Separation and Side-Load Behavior of Truncated Ideal Rocket Nozzles." *AIAA Paper No. 2001-3686*, July 2001.
5. Frey, M.; Hagemann, G.: "Status of Flow Separation Prediction in Rocket Nozzles," *AIAA Paper No. 1998-3619*, July 1998.
6. Hagemann, G., Shock Waves, Proceedings of 26th International Symposium on Shock Waves, 1st ed., Springer Berlin Heidelberg, Germany, 2009, Part 1, pgs 59-66.
7. Hagemann, G., Frey, M., "Shock pattern in the plume of rocket nozzles: needs for design consideration," *26th International Symposium on Shock Waves*, Gottingen, Germany, July 2007.
8. Reijasse, Ph., et al.: "Flow Separation Experimental Analysis in Overexpanded Subscale Rocket-Nozzles," *AIAA Paper No. 2001-3556*, July 2001.
9. Dumnov, G., E.: "Unsteady Side-Loads Acting on the Nozzle With Developed Separation Zone," *AIAA Paper No. 1996-3220*, July 1996.
10. Frey, M.; et al.: "Subscale Nozzle Testing at the P6.2 Test Stand," *AIAA Paper No. 2000-3777*, July 2000.
11. Smith, S., D., "Final Report, Aerospike Design and Performance Tool", Contract ESI-SUB-002 & NAS8-0002, 6 August, 2001. Plumetech, Huntsville, AL., 35805.
12. Dunn, S., S., & Coats, D., E., "TDK02 Two-Dimensional Kinetics Nozzle Performance Program, User Manual", December, 2002, SEA, Inc. Carson City, NV, 89701.
13. Brown, A., M., Ruf, J., H., McDaniels, D., M.,; "Recovering Aerodynamic Side Loads on Rocket Nozzles using Quasi-Static Strain-Gage Measurements," 50th Structures, Structural Dynamics, and Materials Conference, Palm Springs, California, *AIAA Paper No. 2009-2681* May 2009.
14. Kwan, W., Stark, R., "Flow Separation Phenomena in Subscale Rocket Nozzles", AIAA Paper No. 2002-4229, July 2002.